# Journal of Materials Chemistry A



PAPER View Article Online View Journal



Cite this: DOI: 10.1039/d5ta07300f

Received 8th September 2025 Accepted 27th October 2025

DOI: 10.1039/d5ta07300f

rsc.li/materials-a

# Water oxidation to H<sub>2</sub>O<sub>2</sub> on surface-modified carbon cloth electrodes

Xuefei Zhao, <sup>ab</sup> Chenwei Ni, <sup>ab</sup> Qingbo Chang, <sup>abc</sup> Ben Chang, <sup>ab</sup> Pengfei Zhang, <sup>a</sup> Fusai Sun, <sup>ab</sup> Jingying Shi <sup>ab</sup> and Can Li <sup>b</sup>\*\*

The electrochemical water oxidation reaction (WOR) represents a promising route for on-site synthesis of hydrogen peroxide ( $H_2O_2$ ), but its practical application is hindered by limited activity, selectivity, and insufficient mechanistic understanding. Herein, we report a polyvinylidene fluoride-modified carbon cloth (PVDF/CC) electrocatalyst that achieves a faradaic efficiency of 91% toward  $H_2O_2$  at 2.75 V vs. RHE, with a high current density of 131 mA cm<sup>-2</sup> and accumulated  $H_2O_2$  concentration of 52 mM. Through a combination of *in situ* ATR-FTIR spectroscopy and isotope labeling experiments, we confirm the involvement of a carbonate-mediated reaction pathway. Theoretical calculations further reveal that fluorine-induced hydrogen bonds between PVDF and surface hydroxyl groups promote hydroxyl adsorption and facilitate the formation of  $HCO_4^-$  intermediates. This work offers a simple and cost-effective strategy for efficient electrochemical  $H_2O_2$  production *via* the WOR pathway.

#### Introduction

Hydrogen peroxide ( $H_2O_2$ ) serves as an essential chemical in diverse applications from wastewater treatment to industrial synthesis.<sup>1-3</sup> Current anthraquinone oxidation (AO) processes face sustainability challenges due to multi-step operations and significant organic byproduct generation.<sup>1-6</sup> Electrochemical synthesis emerges as a green alternative, where the water oxidation reaction (WOR) offers inherent advantages over the oxygen-dependent oxygen reduction reaction (ORR): a simple operation using only aqueous feedstock.<sup>7-19</sup> However, the WOR faces fundamental limitations: the thermodynamically favored four-electron pathway (OER, eqn (2)) and rapid  $H_2O_2$  decomposition (0.68 V  $\nu s$ . RHE) significantly constrain reaction selectivity and controllability.

$$2H_2O \rightarrow H_2O_2 + 2H^+ + 2e^- \quad E^\theta = 1.76 \text{ V vs. RHE}$$
 (1)

$$2H_2O \rightarrow O_2 + 4H^+ + 4e^- \quad E^\theta = 1.23 \text{ V vs. RHE}$$
 (2)

Current catalysts exhibit performance trade-offs: metal oxides (BiVO<sub>4</sub>, SnO<sub>2</sub>, *etc.*) achieve >90% faradaic efficiency but limited current density (<100 mA cm $^{-2}$ ), <sup>12,15–17,20–23</sup> while modified carbon materials (PTFE/CFP and CNFs) show enhanced activity at the expense of selectivity. <sup>13,14,19,24–32</sup> This limited selectivity comes from three main reasons. First, the  $4e^-$  side

reaction cannot be fully stopped. Second, the surface still gets partially oxidized at high potentials. This leads to non-optimal OH adsorption. Third, strong bubble release causes local  $\rm O_2$  shortage. This value is not a simple "defect". It is the limit of the current "local  $\rm O_2$  enrichment" strategy. Moreover,  $\rm H_2O_2$  accumulation rarely exceeds 30 mM due to insufficient stability. These limitations underscore the need for catalyst design, balancing selective active sites with enhanced mass transport.

We present a PVDF/CC electrocatalyst achieving 131 mA cm<sup>-2</sup> current density with 91% faradaic efficiency for the WOR at 2.75 V vs. RHE, producing 52 mM H<sub>2</sub>O<sub>2</sub> in carbonate/ phosphate electrolytes. Controlled PVDF loading optimizes interfacial interactions, enabling sustained high activity in energy conversion systems. Kinetic analysis reveals dynamic equilibrium between H<sub>2</sub>O<sub>2</sub> generation and decomposition, with derived rate constants explaining concentration stability. Theoretical calculations identify fluorine-hydroxyl hydrogen bonding as the critical mechanism: these bonds enhance hydroxyl adsorption while stabilizing HCO<sub>4</sub> intermediates through active site exposure. The hydroxyl electron transfer step emerges as the rate-limiting barrier governing the reaction potential. This work establishes fundamental principles for designing fluorinated electrocatalysts, providing both mechanistic understanding and practical guidelines for industrial H<sub>2</sub>O<sub>2</sub> synthesis.

#### Results and discussion

A series of carbon cloth electrodes with varying loadings of polyvinylidene fluoride (PVDF) were fabricated by spraying different volumes (0.2–1.0 mL) of PVDF solution, denoted as

<sup>&</sup>quot;State Key Laboratory of Catalysis, Dalian National Laboratory for Clean Energy, Dalian Institute of Chemical Physics, Chinese Academy of Sciences, Dalian 116023, China. E-mail: canli@dicp.ac.cn; jingyingshi@hainanu.edu.cn

<sup>&</sup>lt;sup>b</sup>University of Chinese Academy of Sciences, Beijing 100049, China

School of Chemistry, Dalian University of Technology, Dalian 116024, China

PVDF/CC-1 to PVDF/CC-5. These electrodes were subjected to thorough physicochemical characterization to elucidate the structure–performance relationship.

Morphological and elemental distribution analyses (Fig. 1a and b) provide critical insights into the accessibility of active sites and mass transport properties. Scanning electron microscopy (SEM) images reveal that the pristine carbon cloth consists of smooth, interwoven carbon fibers (left panel of Fig. 1a). With increasing PVDF loading (Fig. S1), a continuous polymer film gradually coats the fiber surfaces. Notably, in the high-loading sample PVDF/CC-5, PVDF not only forms a dense and conformal layer over the fibers but also preferentially fills the inter-fiber junctions. This "bridging" effect is expected to improve the mechanical integrity of the electrode, thereby promoting structural stability during prolonged electrochemical operation—particularly critical for the water oxidation reaction under high potentials. Energy-dispersive X-ray spectroscopy (EDS) mapping (Fig. 1b) confirms the homogeneous distribution of fluorine across the fiber surfaces, attesting to the uniformity and completeness of the PVDF coating.

Crystalline structure analysis was conducted *via* X-ray diffraction (XRD) to identify the phase composition of the modified layer (Fig. 1c). All PVDF-modified electrodes exhibit distinct diffraction peaks at around 18.5° and 20.2°, corresponding to the (020) and (110) planes of crystalline PVDF, respectively. The absence of amorphous halos confirms the successful deposition of crystalline PVDF *via* the spraying method. The gradual enhancement in peak intensity with increasing precursor volume (0.2 to 1.0 mL) further corroborates the controllable loading of PVDF (Fig. S4). The crystalline

nature of PVDF may influence the electronic structure and interfacial charge transfer properties of the electrode, potentially owing to its ferroelectric character.

To probe the surface chemical states and interfacial reactivity, X-ray photoelectron spectroscopy (XPS) was performed on both pristine CC and PVDF/CC-5 samples (Fig. 1d and e). The C 1s spectrum of CC can be fitted with four components: CC (284.8 eV), CO (286.2 eV), C=O (288.0 eV), and a minor contribution from CF (290.9 eV). In contrast, the C 1s spectrum of PVDF/CC-5 deconvolutes into five peaks: graphitic sp<sup>2</sup> carbon (283.4 eV, from the substrate), CC (284.8 eV), CO (285.7 eV), C=O (287.0 eV), and a dominant CF peak at 289.4 eV, characteristic of the -CF<sub>2</sub>- group in PVDF. Consistently, the F 1s spectrum shows a primary signal at 686.7 eV, confirming the formation of CF bonds. Additionally, the O 1s spectra indicate the presence of oxygen-containing functional groups (CO at 530.7 eV and C=O at 532.7 eV), likely introduced during air exposure or pretreatment. These hydrophilic moieties are anticipated to enhance the wettability of the electrode, thereby facilitating reactant diffusion and product release during electrocatalysis. As shown in Fig. 2a, the PVDF/CC composite electrode demonstrates optimal performance for the water oxidation reaction (WOR) at a PVDF loading corresponding to 0.6 mL of precursor solution. In comparison, bare carbon cloth (CC) predominantly facilitates the 4-electron pathway for the WOR, leading to vigorous oxygen evolution evident as continuous bubbling. Modification with PVDF significantly suppresses gas evolution, suggesting a transition in the reaction mechanism. However, excessive PVDF loading (>0.6 mL) results in electrode passivation and a sharp decrease in current density

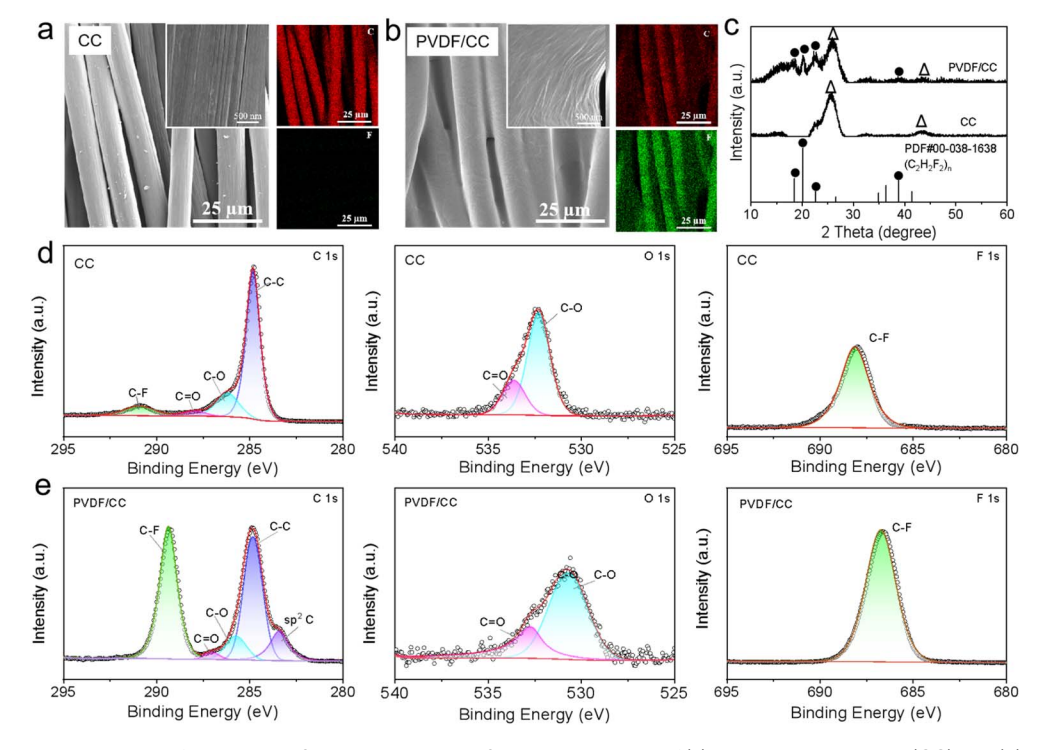


Fig. 1 Structural characterization of electrodes. SEM images and EDS mapping images of (a) pristine carbon cloth (CC) and (b) PVDF/CC. (c) X-ray diffraction (XRD) patterns of CC and PVDF/CC. X-ray photoelectron spectroscopy (XPS) spectra of (d) CC and (e) PVDF/CC.

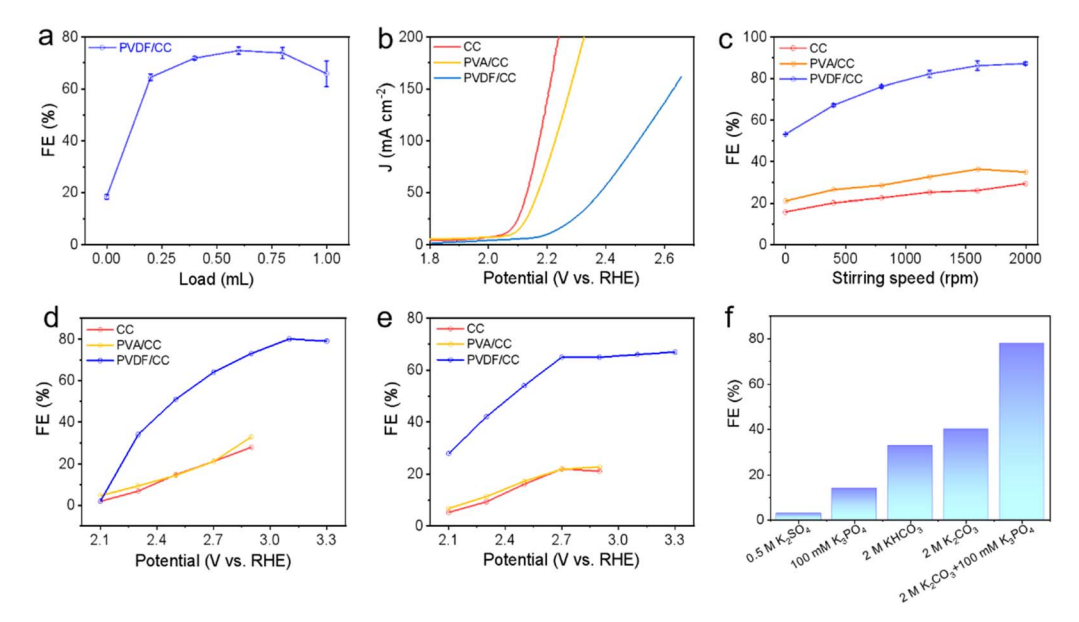


Fig. 2 The electrochemical performance of the WOR process in 2.0 M K<sub>2</sub>CO<sub>3</sub> + 100 mM K<sub>3</sub>PO<sub>4</sub>. (a) FE of PVDF/CC with varying loadings. (b) LSV curves of CC, PVA/CC, and PVDF/CC electrodes. (c) FE of CC, PVA/CC, and PVDF/CC electrodes at different stirring speeds. (d) FE of CC, PVA/C CC, and PVDF/CC electrodes at different applied potentials with a passed charge of 12C. (e) FE of the CC, PVA/CC, and PVDF/CC electrodes after potentiostatic electrolysis for 5 minutes at different applied potentials. (f) FE of the PVDF/CC electrode after passing a charge of 12C in different electrolytes. The tests for (a, c, and f) were conducted at a potential of 2.75 V vs. RHE.

(Fig. S8a), due to insulating polymer overcoating. Therefore, the PVDF/CC-3 sample was selected for further studies to achieve a balance between catalytic activity and electronic conductivity.

The annealing temperature also plays a critical role in determining the electrode performance, with a distinct volcanic trend observed in electrochemical activity (Fig. S8b). The highest WOR efficiency occurs after treatment at 400 °C. When the temperature reaches 500 °C, PVDF decomposes and evaporates (Fig. S2), resulting in a drastic decline in WOR selectivity from 91% to 30%—a threefold reduction bringing performance back to the level of unmodified CC. This complete reversal upon PVDF removal confirms that the modification is a surfacespecific process without altering the bulk structure of carbon cloth, underscoring the stability of the substrate throughout thermal treatment.

The influence of stirring speed on electrode behavior was systematically examined (Fig. S9). Three electrodes—CC, PVA/ CC, and PVDF/CC-exhibited characteristic Faraday efficiency (FE) profiles in response to the agitation intensity (Fig. 2c). The FE increased with stirring speed until reaching a plateau at 1600 rpm, which was adopted as the standard condition. This trend is attributed to the competition between H<sub>2</sub>O<sub>2</sub> generation and its oxidative consumption. In stagnant electrolyte, accumulated H<sub>2</sub>O<sub>2</sub> near the electrode surface undergoes rapid oxidation to O<sub>2</sub>, lowering the FE. Mechanical stirring (>600 rpm) enhances mass transport, shifting H<sub>2</sub>O<sub>2</sub> away from the surface and reducing parasitic oxidation. Notably, PVDF/CC operates at a lower current density while achieving a higher FE compared to CC and PVA/CC (Fig. 2b). This improved performance is ascribed to fluorine-hydroxyl hydrogen bonding within the PVDF layer, which promotes hydroxyl adsorption and stabilizes

the key HCO<sub>4</sub> intermediate, thereby favoring the desired reaction pathway.

We further evaluated FE as a function of applied potential under two distinct protocols: fixed charge and fixed duration (Fig. S10). Under fixed-charge conditions, all electrodes showed an initial rise and subsequent saturation in FE with increasing potential (Fig. 2d and e). PVDF/CC exhibited a substantial enhancement in FE, from 2% to 80%. Higher potentials promote H<sub>2</sub>O<sub>2</sub> formation while curtailing its residence time, thus limiting decomposition. In fixed-duration tests, PVDF/CC reached an FE of 67% at high potential-2.4 times greater than the 28% observed at 2.1 V—highlighting the dual role of potential in both producing and degrading H<sub>2</sub>O<sub>2</sub>. Since H<sub>2</sub>O<sub>2</sub> decomposition depends on both concentration and potential, fixed-charge protocols provide consistent product accumulation and minimize concentration-led artifacts, offering a more reliable comparison than time-based evaluations. The consistent superiority of PVDF/CC across methodologies underscores the role of its interfacial properties in stabilizing reactive species through hydrogen bonding. The potentiostatic method maintains the electrode potential within a "safe window" that favors H<sub>2</sub>O<sub>2</sub> formation. This ensures that the measured current primarily originates from H<sub>2</sub>O<sub>2</sub> production. For comparison, galvanostatic tests were also performed (Fig. S11). The faradaic efficiency obtained from galvanostatic measurements was consistently lower. It never exceeded 75%. This limit does not represent the catalyst's intrinsic capability. Instead, it reflects a limitation of the galvanostatic method. At high current densities, the electrode potential shifts unavoidably. This shift moves the potential outside the safe window. As a result, part of the current oxidizes the formed H<sub>2</sub>O<sub>2</sub> further. This process

systematically underestimates the efficiency. Therefore, we conclude that the faradaic efficiency measured by the potentiostatic method more accurately represents the true selectivity of our catalyst toward  $\rm H_2O_2$  production.

To enhance WOR selectivity, potassium phosphate was introduced as a stabilizer for  $H_2O_2$ . As illustrated in Fig. 2f, WOR selectivity increased from 3% in potassium sulfate to 14% in phosphate electrolyte. Greater improvements were observed in bicarbonate (33%) and carbonate (40%) electrolytes. An optimized mixed carbonate/phosphate electrolyte further increased the selectivity to 78%. These results suggest that carbonate/bicarbonate species promote  $H_2O_2$  generation, while phosphate ions inhibit its decomposition. The synergistic effect among these additives significantly enhances WOR selectivity, providing valuable insights into electrolyte design for efficient oxidation systems.

The PVDF/CC electrode exhibited stable  $H_2O_2$  production during 3.8 h electrolysis, accumulating 52 mM  $H_2O_2$  (Fig. 3a). However, the faradaic efficiency (FE) decreased significantly from 90% to 10% during prolonged operation (Fig. S14), suggesting the progressive dominance of oxygen evolution. This decline occurred because  $H_2O_2$  accumulation accelerated its oxidation rate, establishing a dynamic equilibrium between production and consumption. Consequently, prolonged electrolysis predominantly produced oxygen rather than  $H_2O_2$ . To further investigate the effect of reaction conditions on  $H_2O_2$  synthesis efficiency, we evaluated the electrocatalytic performance at low temperatures (ice bath) (Fig. S12). The results show that the low-temperature condition reduced the reaction

kinetics. This led to a decrease in the current density to about 80 mA cm<sup>-2</sup>. However, it effectively suppressed the decomposition of H<sub>2</sub>O<sub>2</sub>. As a result, the accumulated H<sub>2</sub>O<sub>2</sub> concentration significantly increased to about 60 mM. This phenomenon clearly reveals a key trade-off in the electrocatalytic synthesis of H<sub>2</sub>O<sub>2</sub>. The lower temperature limits the reaction rate. However, it improves the net H<sub>2</sub>O<sub>2</sub> yield by suppressing side reactions. These results provide additional insight into the boundary conditions of the catalyst's performance. Cycle stability tests confirm the durability of PVDF/CC (Fig. 3b). Regular electrolyte replacement at 10 minute intervals maintained consistent WOR activity. The concentration of H2O2 was determined colorimetrically, and a standard calibration curve was established (Fig. S13). To investigate the performance decay of the catalyst during the reaction, we characterized the electrode after the stability test by SEM, XPS, and XRD. The SEM image (Fig. S3) shows localized damage to the PVDF film on the carbon fibers. This indicates a weakening of its physical structure during the reaction. XPS analysis (Fig. S6) further confirms the chemical changes in PVDF/CC. The fluorine content decreased from 47.16% to 39.83%. In contrast, the oxygen content increased from 1.12% to 6.97%. These changes suggest partial oxidation of the electrode. Additionally, XPS detected potassium ions from the electrolyte remaining on the electrode surface. The XRD pattern (Fig. S5) shows no significant shift in diffraction peaks before and after the electrochemical test. This indicates good structural stability of the material during the electrochemical process. No obvious phase change or structural damage occurred. These results collectively demonstrate that

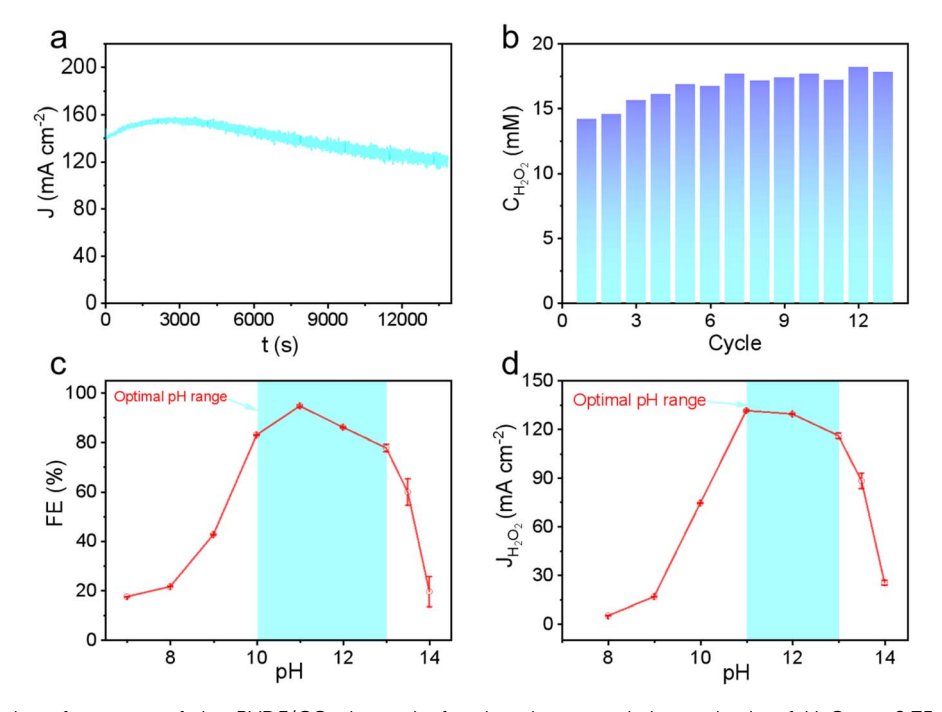


Fig. 3 Electrochemical performance of the PVDF/CC electrode for the electrocatalytic synthesis of  $H_2O_2$  at 2.75 V vs. RHE. (a) Chronoamperometric (current density vs. time) curve during long-term electrolysis. (b) Cycling stability evaluated by monitoring the concentration of produced  $H_2O_2$ . The electrolyte was replaced every 10 minutes to mitigate product accumulation. (c) Faraday efficiency (FE) and (d) partial current density for  $H_2O_2$  production measured in electrolytes with different pH values after passing a charge of 12C.

the decline in catalyst stability is mainly attributed to physical damage and surface chemical changes in the PVDF layer, pHdependent studies (Fig. 3c and d) revealed volcano-shaped trends in both current density and FE, peaking at pH 11-13. The maximum FE reached was 91% within this optimal pH range. A direct comparison with previously reported electrocatalysts for hydrogen peroxide production (Fig. S15) highlights the superior performance of our system. As shown in Fig. S15a, the H<sub>2</sub>O<sub>2</sub> concentration achieved in this work significantly surpasses most literature values. Fig. S15b reveals a higher faradaic efficiency (indicated by red markers), reflecting enhanced reaction selectivity. Furthermore, our catalyst also exhibits an exceptional H<sub>2</sub>O<sub>2</sub> production rate (Fig. S15c). Collectively, these results demonstrate clear advantages in concentration, efficiency, and production rate for electrochemical H<sub>2</sub>O<sub>2</sub> generation.

Fig. 4a shows the change curve of H<sub>2</sub>O<sub>2</sub> concentration with reaction time. Based on the kinetic characteristics, the process can be divided into three distinct stages: (1) rapid growth stage (green), (2) competition stage (yellow), and (3) equilibrium stage (red). In the initial rapid growth stage, the H<sub>2</sub>O<sub>2</sub> concentration in the system is low. The formation rate  $(r_g)$  is significantly higher than the consumption rate  $(r_c)$ , leading to a rapid increase in H<sub>2</sub>O<sub>2</sub> concentration. During the competition stage, the accumulated  $H_2O_2$  concentration causes  $r_c$  to gradually increase. As a result, the net formation rate  $(r_{\text{net}} = r_{\text{g}} - r_{\text{c}})$ decreases significantly. Finally, the system reaches a dynamic equilibrium state. At this stage,  $r_g$  equals  $r_c$ , and the  $H_2O_2$ concentration stabilizes at the equilibrium concentration  $([H_2O_2]_{eq} = 39.1 \text{ mM}, \text{ determined by nonlinear fitting}).$  The concentration of hydrogen peroxide increased with prolonged electrolysis time; however, the faradaic efficiency (FE) decreased (Fig. S14), indicating simultaneous generation and decomposition of H<sub>2</sub>O<sub>2</sub> during the process. The H<sub>2</sub>O<sub>2</sub> concentration over time follows the equation:  $C_{\text{H}_2\text{O}_2} = C_0 \times (1 - \exp(-k \times t))$ . Here,  $C_{H_2O_2}$  is the  $H_2O_2$  concentration (mM) at time t,  $C_0$  is the equilibrium concentration (mM), k is the consumption rate constant  $(\min^{-1})$ , and t is the time (min). To verify the reliability of the equilibrium concentration, a pre-added H<sub>2</sub>O<sub>2</sub> control experiment was conducted. The results show that when the initial  $H_2O_2$  concentration is high ( $[H_2O_2]_{initial} > [H_2O_2]_{eq}$ ), the system undergoes a rapid consumption stage and a competition stage before reaching the same equilibrium concentration. This result is highly consistent with the forward reaction experiment, confirming the reliability of the established kinetic model. Fig. 4b shows a comparative study of the dynamic changes in H<sub>2</sub>O<sub>2</sub> concentration under electrolysis and static conditions. Under electrolysis, the H2O2 concentration exhibits three distinct stages: (1) a rapid consumption phase (red), (2) a competition phase (yellow), and (3) an equilibrium phase (green). In contrast, under static conditions, the H<sub>2</sub>O<sub>2</sub> concentration decreases monotonically over time. The decomposition rate under static conditions is significantly lower than that under electrolysis. Kinetic analysis reveals that H2O2 decomposition under static conditions follows a first-order reaction model:  $C_{H,O_2} = C_0 \times \exp(-k \times t)$ . Here,  $C_{H,O_2}$  is the  $H_2O_2$ concentration (mM) at time t,  $C_0$  is the initial concentration (mM), k is the apparent degradation rate constant (min<sup>-1</sup>), and t is the reaction time (min).

In the electrocatalytic water oxidation reaction for H2O2 synthesis, carbonate ions (CO<sub>3</sub><sup>2-</sup>) significantly influence the reaction kinetics. The reaction order with respect to carbonate concentration, measured using a PVDF/CC electrode, was determined to be 0.85 (Fig. 5a), indicating a strong dependence of the reaction rate on the carbonate concentration. This suggests that carbonate is likely involved in the rate-determining step or the formation of key intermediates, supporting a mechanism wherein carbonate mediates the reaction pathway via peroxocarbonate intermediates such as  $HCO_4^-$  or  $C_2O_6^{2-}$ .

To verify this mechanism, an isotope tracing experiment was conducted. After adding H<sub>2</sub><sup>18</sup>O to the electrolyte, the <sup>18</sup>O abundance in carbonate species increased by 7.4 times in the electrolyzed sample compared to the non-electrolyzed control (Fig. 5b), indicating rapid oxygen exchange between water and carbonate during electrolysis and confirming the active participation of carbonate in the reaction process.

To further investigate the reaction pathway, in situ ATR-FTIR spectroscopy was employed to monitor intermediate species on

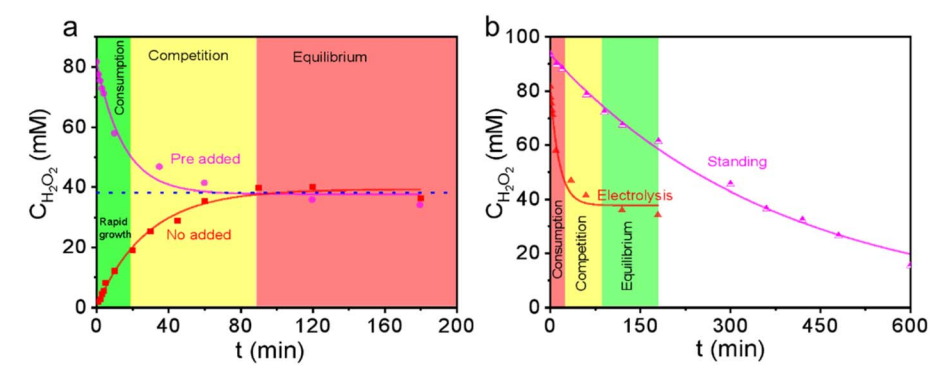


Fig. 4 Kinetic analysis of H<sub>2</sub>O<sub>2</sub> electrogeneration and decomposition on the PVDF/CC electrode. (a) Time-dependent concentration profiles of H<sub>2</sub>O<sub>2</sub> during potentiostatic electrolysis at 2.75 V vs. RHE from electrolytes without initial H<sub>2</sub>O<sub>2</sub> and with excessive added H<sub>2</sub>O<sub>2</sub>. Data points represent experimental measurements, and solid lines correspond to the kinetic fitting curves. (b) Comparative evaluation of  $H_2O_2$  concentration evolution: electrolysis in the presence of excessive initial  $H_2O_2$  and spontaneous chemical decomposition of  $H_2O_2$  in the absence of electrolysis. All experiments were conducted in a 2.0 M K<sub>2</sub>CO<sub>3</sub> + 100 mM K<sub>3</sub>PO<sub>4</sub> electrolyte solution.

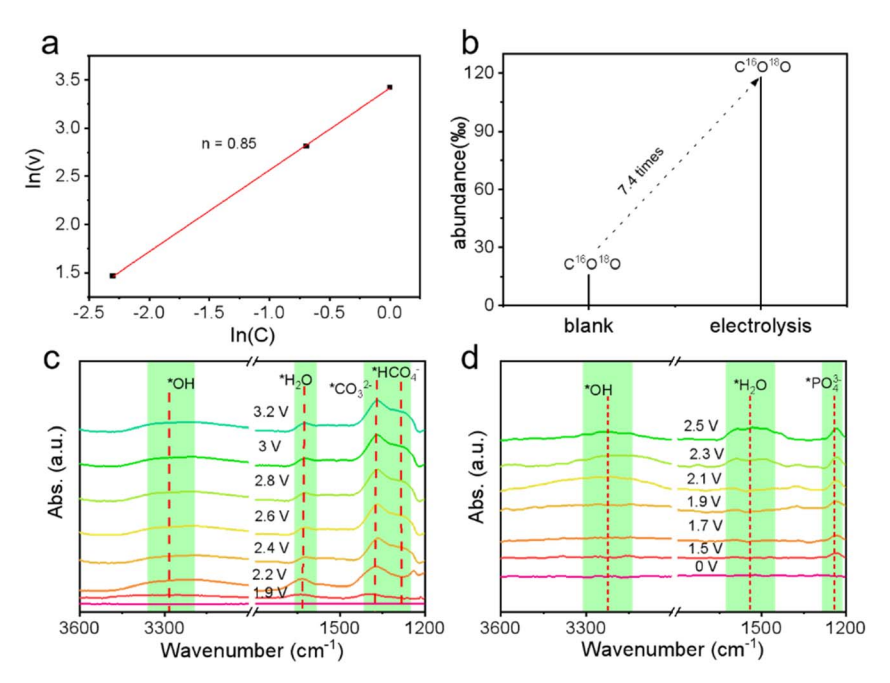


Fig. 5 Mechanistic investigations of the  $H_2O_2$  generation pathway on the PVDF/CC electrode. (a) Determination of the reaction order with respect to  $CO_3^{2-}$  concentration. (b) Isotope tracing analysis: detection of  $^{18}O$  in the evolved  $CO_2$  product from electrolysis in  $H_2^{18}O$ -enriched electrolyte. *In situ* electrochemical ATR-FTIR spectra of the PVDF/CC electrode surface during electrolysis in (c) 2.0 M  $K_2CO_3$  and (d) 2.0 M  $K_3PO_4$  electrolytes, revealing potential-dependent adsorbed species.

the PVDF/CC electrode surface in real time (Fig. 5c). As the potential increased, the water oxidation reaction accelerated, as evident from the enhanced signal at ~1630 cm<sup>-1</sup> corresponding to the H-O-H bending vibration of water.33 Simultaneously, a peak appeared at  $\sim$ 1400 cm<sup>-1</sup> attributed to the C-O stretching vibration of adsorbed carbonate species. Notably, a characteristic peak observed at 1296 cm<sup>-1</sup> is assigned to peroxocarbonate species (e.g., HCO<sub>4</sub><sup>-</sup>), resulting from the coupling of C-O and C=O vibrational modes-a definitive fingerprint for such intermediates-confirming their formation on the electrode surface.34 To ascertain the necessity of carbonate, a control experiment was performed in potassium phosphate electrolyte (Fig. 5d). The characteristic peaks at 1400 cm<sup>-1</sup> and 1296 cm<sup>-1</sup> were completely absent, indicating that the formation of these intermediates strictly depends on the presence of carbonate. Collectively, these experimental results demonstrate that carbonate ions act as essential mediators in the electrocatalytic water oxidation reaction for hydrogen peroxide production, facilitating H<sub>2</sub>O<sub>2</sub> generation through the formation of peroxocarbonate intermediates.

Through theoretical calculations, we elucidated the detailed reaction mechanism of the PVDF/CC anode in catalyzing water oxidation to produce  $H_2O_2$ , confirming its high activity and selectivity. The proposed mechanism involves the following key steps: (1) adsorption of hydroxide (OH $^-$ ) onto the surface; (2) electron transfer from the adsorbed hydroxide to form a hydroxyl radical (\*OH); (3) nucleophilic attack of the hydroxyl radical by carbonate ions ( $CO_3^{2-}$ ) to form the  $HCO_4^-$  intermediate; and (4) hydrolysis of  $HCO_4^-$  in alkaline solution to produce  $H_2O_2$ .

Using Gaussian software, we calculated the key intermediates involved in the reaction pathway, including five critical configurations: (I) bare PVDF/CC surface, (II) PVDF/CC with adsorbed OH-, (III) PVDF/CC with a surface hydroxyl radical, (IV) the HCO<sub>4</sub><sup>-</sup> intermediate, and (V) the final H<sub>2</sub>O<sub>2</sub> product. Based on Nørskov theory,35 a reaction free energy diagram was constructed (Fig. 6a). Calculations were performed using the 6-31g(d) basis set and B3LYP functional, with implicit solvent corrections to account for aqueous conditions. All calculations were conducted at 298.15 K and 1 atm with corrections for free energy.36 The electronic energies, zero-point energies, entropies, and free energies of all species are listed in the SI tables. The free energy diagram shows that the step involving electron transfer from the surface hydroxide to form the hydroxyl radical has the highest energy barrier, which correlates with the experimental observation of significant H<sub>2</sub>O<sub>2</sub> activity occurring only beyond 2.7 V (vs. RHE, pH = 12.6).

A detailed analysis of reaction steps reveals that fluorine atoms in PVDF significantly lower the energy of OH $^-$  adsorption by interacting with surface hydroxides (Fig. 6b). The adsorbed OH $^-$  group sits 1.46 Å from the CC surface, while hydrophobic CC regardless of PVDF modification fails to adsorb carbonate ions. Based on this, we propose that hydroxide ions adsorb first and undergo electron transfer, rather than directly interacting with carbonate. The transition state searches validated reaction pathways for steps III  $\rightarrow$  IV and IV  $\rightarrow$  V. The III  $\rightarrow$  IV step involves a second electron transfer to form HCO $_4^-$ , with a transition state (ts\_III-IV) exhibiting an imaginary frequency of -503.63 Hz and a 0.65 eV energy barrier (Fig. 6c). Similarly, the IV  $\rightarrow$  V step (HCO $_4^-$  hydrolysis to H $_2$ O $_2$ ) has a transition state

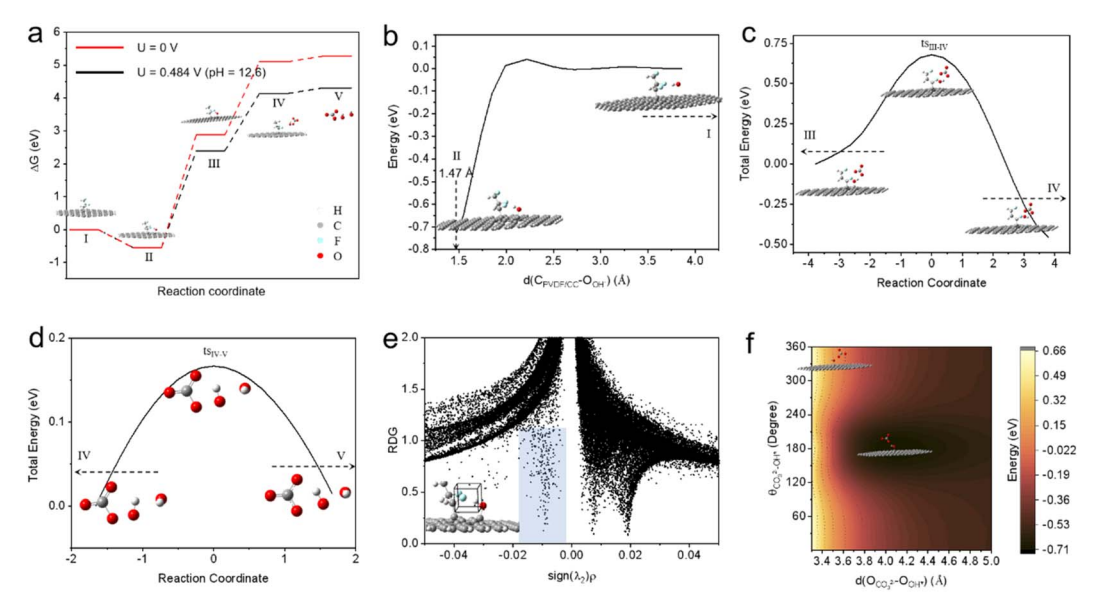


Fig. 6 Reaction energy diagram and structural insights into the catalytic mechanism of PVDF/CC for H<sub>2</sub>O<sub>2</sub> production. (a) Reaction free energy diagram for key steps, highlighting configurations IV. (b) Energy profile of OH<sup>-</sup> adsorption on PVDF/CC, with the x-axis showing the OH<sup>-</sup> distance from the CC surface. (c) Intrinsic reaction coordinate (IRC) scan for the tsIII-IV transition state, representing the reaction between hydroxyl radicals and carbonate ions to form HCO<sub>4</sub><sup>-</sup>. (d) IRC scan for the tsIV-V transition state, representing the hydrolysis of HCO<sub>4</sub><sup>-</sup> to form H<sub>2</sub>O<sub>2</sub>. (e) NCI analysis of hydrogen bonding between PVDF fluorine and hydroxyl groups, showing strong interactions. The blue regions in the plot represent the hydrogen bonding interaction zones. (f) Energy surface comparison showing enhanced carbonate attack and HCO<sub>4</sub> formation on CC surfaces.

 $(ts_{IV-V})$  with an imaginary frequency of -346.51 Hz and a 0.15 eV barrier (Fig. 6d). These results support the proposed pathway.

To investigate the role of the fluorine groups in PVDF and their interactions with the surface hydroxyl groups, noncovalent interaction (NCI) analysis37 was performed (see Computational details method in SI). By selecting the geometric midpoint between the hydrogen of the hydroxyl group and the fluorine in PVDF within a cubic region of side length of 2 bohr, we plotted the reduced density gradient (RDG) *versus* sign $(-\lambda_2)\rho$ (Fig. 6e). The analysis reveals significant hydrogen bonding interactions in this region, with a sign $(-\lambda_2)\rho$  value of approximately -0.01, indicating strong hydrogen bonding. These hydrogen bonds not only stabilize the adsorption of hydroxyl groups but also expose the active oxygen sites, facilitating the nucleophilic attack by carbonate ions to form the HCO<sub>4</sub> intermediate.

To verify the role of fluorine-induced hydrogen bonds in stabilizing key reaction intermediates, we combined experimental and theoretical evidence. At the experimental level, no clear C-F vibration signals were directly observed in Raman spectroscopy (Fig. S7). This was due to strong background fluorescence from the carbon support. It also suggests that PVDF may exist in a highly dispersed amorphous state. This state favors the exposure of fluorine atoms. Key indirect evidence came from a fluorine-free control experiment. The PVA/CC sample showed significantly reduced activity and selectivity in H<sub>2</sub>O<sub>2</sub> electrosynthesis (Fig. 2b-e). This result experimentally confirms that fluorine species are essential for achieving high performance. At the theoretical level, we obtained direct molecular-level evidence. RDG analysis (Fig. 6e)

shows significant hydrogen bonding between hydroxyl hydrogen atoms and fluorine atoms in the PVDF region. The  $(\lambda^2)$  $\rho$  value is about -0.01. These hydrogen bonds stabilize the adsorption configuration of hydroxyl groups. They also expose active oxygen sites by modulating the local electronic structure. This promotes nucleophilic attack by carbonate ions and the formation of HCO<sub>4</sub> intermediates. Direct experimental observation of transient hydrogen bonds at the electrode/electrolyte interface remains a challenge for future research. However, the current theoretical and experimental evidence are highly consistent. Together, they form a complete evidence chain. This strongly supports the conclusion that fluorine-induced hydrogen bonding is the core mechanism for the high selectivity of this catalytic system.

PVDF modification was further examined via potential energy scans of carbonate-hydroxyl radical interactions on CC (Fig. 6f). Without PVDF, hydroxyl radicals form weak hydrogen bonds (CCOH···O=CO=O<sup>2-</sup>), insufficient for HCO<sub>4</sub><sup>-</sup>. In contrast, PVDF modification enhances interactions, exposing active oxygen for carbonate attack. The calculated ts III-IV infrared spectrum (Fig. S16) matches the experimental FTIR one, validating the model. In summary, the high activity and selectivity of PVDF/CC in water oxidation and H<sub>2</sub>O<sub>2</sub> production stem from hydrogen bonds between fluorine in PVDF and hydroxyl groups on the surface. These bonds stabilize hydroxyl adsorption and reveal active sites for HCO<sub>4</sub><sup>-</sup> formation. The electron transfer step of surface hydroxyls presents the highest energy barrier, determining the reaction potential. A proposed reaction pathway is illustrated in Fig. S17. This schematic diagram clearly shows the microscopic process. In this process,

Paper

fluorine-induced hydrogen bonds stabilize the  $\mathrm{HCO_4}^-$  intermediate. This visualization provides a clear picture for understanding the high selectivity of our system. This study provides critical insights for optimizing PVDF/CC and similar systems for industrial use. Through thorough experiments and calculations, we clarified the role and mechanism of carbonate in the WOR, laying a solid foundation for future research.

#### Conclusions

In conclusion, this work presents a high-performance PVDF/CC anode for electrochemical H2O2 production via the water oxidation reaction (WOR), achieving an FE of 91% at 131 mA cm<sup>-2</sup> with excellent operational stability, underscoring its potential for scalable application. Mechanistic investigations reveal that H2O2 formation follows a carbonate-mediated indirect pathway, wherein PVDF/CC facilitates OH activation to generate ·OH radicals, which subsequently react with carbonate species to form percarbonate intermediates prior to hydrolysis into H<sub>2</sub>O<sub>2</sub>. Theoretical calculations further demonstrate that the enhanced catalytic performance originates from fluorineinduced hydrogen bonding between PVDF and surface hydroxyl species, which strengthens hydroxyl adsorption and promotes the exposure of active sites conducive to HCO4intermediate formation. By integrating experimental and computational approaches, this study elucidates the critical role of carbonate chemistry in the WOR process, providing a fundamental framework for the design of efficient electrochemical systems for H<sub>2</sub>O<sub>2</sub> production.

#### Author contributions

Xuefei Zhao wrote the manuscript and conducted most experiments. Chenwei Ni conducted DFT calculations. Qingbo Chang discussed the concentration detection methods and isotope testing. Ben Chang discussed the analysis and fitting of kinetic data. Pengfei Zhang assisted in guiding *in situ* electrochemical infrared testing. Fusai Sun conducted the EDS test. Jingying Shi directed the work. Can Li revised the manuscript and supervised the work. All authors discussed and revised the manuscript.

#### Conflicts of interest

The authors declare no conflict of interest.

### Data availability

The data supporting this article have been included as part of the supplementary information (SI). Supplementary information is available. See DOI: https://doi.org/10.1039/d5ta07300f.

## Acknowledgements

This work was financially supported by the National Natural Science Foundation of China (No. 22072152, 22472172 and 22090034) and the National Key R&D Program of China (No.

2021YFB4000304). This work was also conducted at the Fundamental Research Center of Artificial Photosynthesis, financially supported by the National Natural Science Foundation of China under Grant No. 22088102.

#### Notes and references

- 1 J. M. Campos-Martin, G. Blanco-Brieva and J. L. G. Fierro, *Angew. Chem., Int. Ed.*, 2006, **45**, 6962–6984.
- 2 Y. Kon, Y. Kimishima, K. Murata and K. Sayama, *RSC Adv.*, 2025, **15**, 4369–4376.
- 3 H. Zhang, Y. Zhang, Q. Wu and C. Ma, *Mater. Lett.*, 2024, 357, 135715.
- 4 Z. Zhang, L. Cui, B. Chen, L. Zhang, C. He, C. Shu, H. Kang, J. Qiu, W. Jing and K. K. Ostrikov, *Energy Environ. Sci.*, 2024, 17, 655.
- 5 Y. Tian, M. Li, Z. Wu, Q. Sun, D. Yuan, B. Johannessen, L. Xu, Y. Wang, Y. Dou, H. Zhao and S. Zhang, *Angew. Chem., Int. Ed. Engl.*, 2022, **61**, e202213296.
- 6 H. Li, B. Zheng, Z. Pan, B. Zong and M. Qiao, Front. Chem. Sci. Eng., 2018, 12, 124–131.
- 7 F. Sun, C. Yang, Z. Qu, W. Zhou, Y. Ding, J. Gao, G. Zhao, D. Xing and Y. Lu, *Appl. Catal.*, B, 2021, 286, 119860.
- 8 D. K. Singh, V. Ganesan, D. K. Yadav, M. Yadav, P. K. Sonkar and R. Gupta, *Catal. Sci. Technol.*, 2021, 11, 1014–1026.
- 9 W. Liu, C. Li, G. Ding, G. Duan, Y. Jiang and Y. Lu, J. Materiomics, 2022, 8, 136–143.
- 10 E. Jung, H. Shin, B. H. Lee, V. Efremov, S. Lee, H. S. Lee, J. Kim, W. Hooch Antink, S. Park, K. S. Lee, S. P. Cho, J. S. Yoo, Y. E. Sung and T. Hyeon, *Nat. Mater.*, 2020, 19, 436–442.
- 11 K. Fuku, Y. Miyase, Y. Miseki, T. Gunji and K. Sayama, *ChemistrySelect*, 2016, 1, 5721–5726.
- 12 X. Shi, S. Siahrostami, G. L. Li, Y. Zhang, P. Chakthranont, F. Studt, T. F. Jaramillo, X. Zheng and J. K. Norskov, *Nat. Commun.*, 2017, **8**, 701.
- 13 S. Mavrikis, M. Göltz, S. C. Perry, F. Bogdan, P. K. Leung, S. Rosiwal, L. Wang and C. Ponce de León, ACS Energy Lett., 2021, 2369–2377.
- 14 S. Mavrikis, M. Goeltz, S. Rosiwal, L. Wang and C. Ponce de Leon, *ACS Appl. Energy Mater.*, 2020, 3, 3169–3173.
- 15 L. Li, Z. Hu and J. C. Yu, Angew Chem. Int. Ed. Engl., 2020, 59, 20538–20544.
- 16 S. Y. Park, H. Abroshan, X. Shi, H. S. Jung, S. Siahrostami and X. Zheng, ACS Energy Lett., 2019, 4, 352–357.
- 17 S. R. Kelly, X. Shi, S. Back, L. Vallez, S. Y. Park, S. Siahrostami, X. Zheng and J. K. Nørskov, ACS Catal., 2019, 9, 4593–4599.
- 18 Z. Wang, K. Li, J. Hu, A. Li, Y. Tang, Y. Sun, P. Wan, H. Jiang and Y. Chen, *Adv. Funct. Mater.*, 2025, 35, 2425301.
- 19 U. Javed, M. Tebyetekerwa, C. Tang, X. Zeng, Z. Wang, K. Sun, J. Yang, I. Marriam, L. Guo, X. Sun, A. K. Sahu, Y. Zhang, A. Zamyadi, A. Du, Q. Li, T. E. Rufford and X. Zhang, Adv. Mater., 2025, 37, 2500834.
- 20 L. Li, K. Xiao, P. K. Wong, Z. Hu and J. C. Yu, *ACS Appl. Mater. Interfaces*, 2022, **14**, 7878–7887.

- 21 J. Baek, Q. Jin, N. S. Johnson, Y. Jiang, R. Ning, A. Mehta, S. Siahrostami and X. Zheng, Nat. Commun., 2022, 13, 7256.
- 22 L. Li, L. Xu, A. W. M. Chan, Z. Hu, Y. Wang and J. C. Yu, Chem. Mater., 2021, 34, 63-71.
- 23 J. Li, D. Solanki, Q. Zhu, X. Shen, G. Callander, J. Kim, Y. Li, H. Wang and S. Hu, J. Mater. Chem. A, 2021, 9, 18498-18505.
- 24 C. Ling, A. Liang, C. Li and W. Wang, J. Zhejiang Univ., Sci. A., 2023, 24, 377-386.
- 25 C. Ling, A. Liang, C. Li and W. Wang, Chem. Eng. J., 2023, 465, 142903.
- 26 Y. Sun, X. Chen, S. Ning, W. Zhou, Z. Yang, J. Cui, D. Wang, J. Ye and L. Liu, J. Mater. Chem. A, 2021, (9), 23994-24001.
- 27 S. Mavrikis, M. Goltz, S. Rosiwal, L. Wang and C. P. de Leon, ChemSusChem, 2022, 15, e202102137.
- 28 C. Xia, S. Back, S. Ringe, K. Jiang, F. H. Chen, X. M. Sun, S. Siahrostami, K. R. Chan and H. T. Wang, Nat. Catal., 2020, 3, 125-134.

- 29 Y. Ando, Int. J. Hydrogen Energy, 2004, 29, 1349-1354.
- 30 Y. Zhang, X. Niu, Z. Lin, D. Zhang, Y. Zheng, M. Huang, C. Jin and J. Zhang, ACS Appl. Nano Mater., 2025, 8, 3356-3367.
- 31 K. Yi, C. Li, S. Hu, X. Yuan, B. E. Logan and W. Yang, Nat. Commun., 2025, 16, 1893.
- 32 X. Song, Y. Wan, Q. Yang, J. Zhang, Y. Zhang, Z. Sun, S. Li, J. Zhang, X. Zhang, S. Ciampi and L. Zhang, J. Am. Chem. Soc., 2025, 147, 22864-22872.
- 33 X. Hu, G. Mei, X. Chen, J. Liu, B. Y. Xia and B. You, Angew. Chem., Int. Ed. Engl., 2023, 62, e202304050.
- 34 L. Li, Z. Hu, Y. Kang, S. Cao, L. Xu, L. Yu, L. Zhang and J. C. Yu, Nat. Commun., 2023, 14, 1890.
- 35 J. K. Nørskov and U. Stimming, J. Electrochem. Soc., 2005, 152, J23.
- 36 T. Lu and O. Chen, Comput. Theor. Chem., 2021, 1200.
- 37 E. R. Johnson, S. Keinan, A. J. Cohen and W. Yang, J. Am. Chem. Soc., 2010, 132, 6498-6506.